J. Fluid Mech. (2004), *vol.* 503, *pp.* 345–355. © 2004 Cambridge University Press
DOI: 10.1017/S0022112004007943 Printed in the United Kingdom

On the physical mechanisms of drag reduction in a spatially developing turbulent boundary layer laden with microbubbles

By ANTONINO FERRANTE AND SAID ELGHOBASHI

Department of Mechanical and Aerospace Engineering, University of California, Irvine, CA 92697, USA

(Received 20 October 2003 and in revised form 22 December 2003)

The objective of this paper is to explain, in as much detail as possible, the physical mechanisms responsible for the reduction of skin friction in a microbubble-laden spatially developing turbulent boundary layer over a flat plate, for $Re_\theta = 1430$. Our DNS results with microbubble volume fraction ranging from $\phi_v = 0.001$ to 0.02 show that the presence of bubbles results in a *local* positive divergence of the fluid velocity, $\nabla \cdot \boldsymbol{U} > 0$, creating a positive mean velocity normal to (and away from) the wall which, in turn, reduces the mean streamwise velocity and displaces the quasi-streamwise longitudinal vortical structures away from the wall. This displacement has two main effects: (i) it increases the spanwise gaps between the wall streaks associated with the sweep events and reduces the streamwise velocity in these streaks, thus reducing the skin friction by up to 20.2% for $\phi_v = 0.02$; and (ii) it moves the location of peak Reynolds stress production away from the wall to a zone of a smaller transverse gradient of the mean streamwise velocity (i.e. smaller mean shear), thus reducing the production rate of turbulence kinetic energy and enstrophy.

1. Introduction

Experimental evidence obtained during the past three decades indicates that injection of gaseous microbubbles (diameter ranging from 1 to 1000 microns, and at a relatively large volume fraction (up to $\phi_v = 0.7$)) into a liquid turbulent boundary layer (TBL) over a flat plate (Madavan, Deutsch & Merkle 1984; Pal, Merkle & Deutsch 1988) or over axisymmetrical bodies (Deutsch & Pal 1990; Clark III & Deutsch 1991) can reduce the skin friction by as much as 80% from its value without bubble injection. However, the basic physical mechanisms responsible for that reduction are not yet fully understood.

The first experimental study of the effect of microbubbles on skin friction was performed by McCormick & Bhattacharyya (1973). Their hydrogen microbubbles were produced by electrolysis via a copper wire wound around a towed body of revolution. The complexity of the flow did not allow discrimination between the effects of skin friction and form drag. Madavan *et al.* (1984) reviewed the experimental work performed by a group of Soviet scientists during the 1970s on skin friction reduction by microbubbles. The optical (laser) and photographic measurements of Pal *et al.* (1988) were conducted for a TBL flow ($3 \times 10^3 \leqslant Re_\theta \leqslant 10^4$) over a flat plate mounted in a water tunnel. The orientation in which buoyancy causes bubbles to rise out of the boundary layer is referred to as the *plate-on-bottom* case, while for the case of *plate-on-top* the tunnel was rotated 180°. These measurements showed the existence

https://doi.org/10.1017/S0022112004007943 Published online by Cambridge University Press

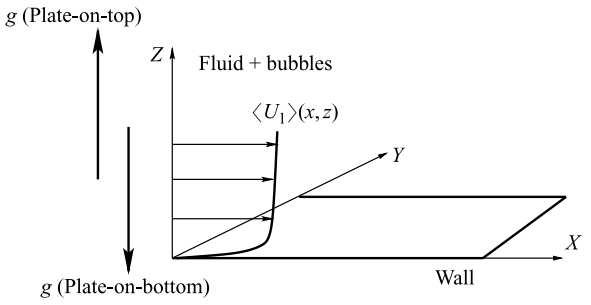


FIGURE 1. Schematic of bubble-laden turbulent boundary layer flow over a flat wall.

of a clear, bubble-free water region between the bubble cloud and the plate for the plate-on-bottom case. The clear water region did not occur in the plate-on-top case. Hence, it was concluded that the clear water region was the result of buoyancy, rather than viscous lift. The spreading rate of the TBL was larger for the plate-on-bottom configuration, demonstrating that buoyancy is a factor, but the persistence of spreading for the plate-on-top configuration where buoyancy inhibited such motion indicated that turbulent diffusion was also significant.

Recently, Xu, Maxey & Karniadakis (2002) performed a direct numerical simulation (DNS) of a fully developed turbulent channel flow ($Re = 3000$) laden with bubbles to study drag reduction. The volume fraction of bubbles, ϕ_v, varied between 0.04 and 0.08. The ratio of bubble radius to the channel half-height ranged from 0.1 to 0.3. The bubbles were injected in two layers parallel to the wall and at distances of $y^+ = 20$ and $y^+ = 54$. The number of bubbles in the flow ranged from 60 to 1600. Buoyancy effects were neglected. Xu *et al.* stated that their results "point to at least three mechanisms involved: one linked to the initial seeding of the bubbles, the second associated with the density effects, where the bubbles reduce the turbulent momentum transfer, and the third governed by specific correlations between the bubbles and the turbulence" and added that "the streaks seem to be affected very little for the cases we investigated here and they became slightly more disorderly due to the chaotic forcing imposed by the bubbles."

Our objective in the present paper is to explain, in as much detail as possible, the physical mechanisms responsible for the reduction of skin friction in a microbubble-laden spatially developing turbulent boundary layer over a flat plate, for $Re_\theta = 1430$.

2. Mathematical description

Figure 1 shows a schematic of the TBL flow where the gravitational acceleration vector is perpendicular to the wall, but it can be pointing either downwards (plate-on-bottom) or upwards (plate-on-top).

We employ the Eulerian–Lagrangian approach in which we solve the fluid continuity and momentum equations in an Eulerian framework, (2.1) and (2.2) below, whereas the bubble acceleration equation, (2.3), is solved for each bubble to track its trajectory in time. We treat the bubbles as rigid spheres, under the assumption of 'dirty' bubbles, i.e. in a non-purified water the gas–liquid interface is solidified, owing to the presence of impurities. We consider air bubbles, with diameter smaller than 1 mm, such that they act like undeformable spheres (Weber number, $We \ll 1$); and we assume that the density of the bubble gas, ρ_b, is negligible compared to that of the surrounding liquid (water), ($\rho \gg \rho_b \approx 0$). Thus, the bubbles are assumed to be massless spheres. The

https://doi.org/10.1017/S0022112004007943 Published online by Cambridge University Press

$\check{\delta}_0$	$\check{U}_\infty$	$\check{\nu}$	$\check{g}$	$\check{d}_b$	d_b^+	τ_b^+	V_t/U_∞	$V_t/u_{rms,0}$
9.7 mm	0.83 m s^{-1}	10^{-6} m^2 s^{-1}	9.81 m s^{-2}	62 μm	2.4	0.157	2.52×10^{-3}	0.08

TABLE 1. Fluid and bubble properties.

bubble equation of motion, (2.3), includes terms representing the added-mass, carrier fluid inertia, Stokes drag, buoyancy (Maxey & Riley 1983), and the lift force (Auton 1987). The equations governing the motion of a spatially developing bubble-laden TBL can be written in non-dimensional form as (Ferrante 2004):
carrier fluid continuity,

$$\partial_t(1-C) + \partial_j[(1-C)\,U_j] = 0; \tag{2.1}$$

carrier fluid momentum,

$$\partial_t[(1-C)U_i] + \partial_j[(1-C)U_iU_j] = -\partial_i[(1-C)p] + \nu\,\partial_j[(1-C)(\partial_jU_i + \partial_iU_j)] - f_i + (1-C)g_i; \tag{2.2}$$

bubble acceleration,

$$\frac{\mathrm{d}V_i}{\mathrm{d}t} = 3\frac{\mathrm{D}U_{s,i}}{\mathrm{D}t} + \frac{1}{\tau_b}(U_{s,i} - V_i + V_t) + [(\boldsymbol{U}_s - \boldsymbol{V}) \times \boldsymbol{\omega}_s]_i. \tag{2.3}$$

In the above equations, U_i are the components of instantaneous fluid (liquid) velocity and p is the pressure. $C(x, y, z, t)$ is the instantaneous local bubble-phase concentration (or volume fraction) computed from the local number of bubbles N_b in a given computational cell of volume, $\mathscr{V}_c$, as

$$C(\boldsymbol{x}, t) = N_b(\boldsymbol{x}, t)\,[\pi d_b^3/6] \,/\, \mathscr{V}_c(\boldsymbol{x}), \tag{2.4}$$

where d_b is the bubble diameter. Equation (2.4) is valid for the condition $d_b/(2L) \ll 1$, where L is the macroscopic length scale of variation of the bubble number density $N_b/\mathscr{V}_c$ (Prosperetti & Zhang 1995). The dimensionless kinematic viscosity is $\nu = 1/Re_\delta$, where $Re_\delta = \check{U}_\infty\check{\delta}_0/\check{\nu}$ is the Reynolds number based on the dimensional free-stream velocity $\check{U}_\infty$, the boundary layer thickness $\check{\delta}_0$ at the inlet plane ($x = 0$) of the computational domain, and the kinematic viscosity $\check{\nu}$. All variables in (2.1)–(2.3) are non-dimensionalized by $\check{U}_\infty$ and $\check{\delta}_0$ (table 1). The force f_i in (2.2) is imparted by the bubbles to the surrounding fluid, and is calculated according to Druzhinin & Elghobashi (1998) as

$$-f_i = C\left(\frac{\mathrm{D}U_{s,i}}{\mathrm{D}t} - g_i\right), \tag{2.5}$$

where g_i is the component of the gravitational acceleration in the i-direction; $g_i = -g\delta_{iz}$ for the plate-on-bottom configuration, whereas $g_i = g\delta_{iz}$ for the plate-on-top case (figure 1), where g is the dimensionless gravitational acceleration.

In (2.3), $\boldsymbol{U}_s$ and $\boldsymbol{\omega}_s$ are respectively the instantaneous fluid velocity and fluid vorticity at the bubble location, $\boldsymbol{x}_b(t)$, and $\boldsymbol{V}$ is the bubble instantaneous velocity; $\mathrm{d}/\mathrm{d}t \equiv \partial_t + V_j\partial_j$ is the time derivative in a frame moving with the bubble, $\mathrm{D}/\mathrm{D}t \equiv \partial_t + U_j\partial_j$ is the time derivative following a fluid element. The bubble response time τ_b is defined according to Stokes drag law as $\tau_b = d_b^2\,/\,(36\,\nu)$. The terminal velocity $V_t = -2\tau_b g_i$. Throughout the paper, dimensionless quantities in wall units carry the

https://doi.org/10.1017/S0022112004007943 Published online by Cambridge University Press

L_x	L_y	L_z	L_x^+	L_y^+	L_z^+	N_x	N_y	N_z	Δx^+	Δy^+	z_{min}^+
$20\,\delta_0$	$5\,\delta_0$	$3.6\,\delta_0$	7424	1856	1336	512	256	96	14.5	7.25	0.58

TABLE 2. Computational mesh details.

superscript $^+$, i.e. $U_1^+ = U_1/u_\tau$, $z^+ = z\,u_\tau/\nu$ and $t^+ = t\,u_\tau^2/\nu$, where u_τ is the wall friction velocity.

The computational domain is a parallelepiped whose dimensions L_x, L_y and L_z, and the corresponding numbers of grid points, N_x, N_y and N_z in the streamwise, spanwise and wall-normal directions respectively are listed in table 2. The computational mesh is equispaced in the streamwise and spanwise directions, with grid spacings Δx^+ and Δy^+ (table 2), whereas in the vertical direction, the mesh is stretched gradually via mapping a uniform computational grid ζ into its non-uniform counterpart z with a combination of hyperbolic tangent functions (Ferrante & Elghobashi 2004) with the closest grid point to the wall located at $z_{min}^+ = 0.58$.

The initial ($t = 0$) velocity field of the fluid throughout the domain was identical to the instantaneous velocity field ($t^+ = 2600$) computed by DNS of the single-phase TBL ($\phi_v = 0$) on the same mesh (table 2). The generation of the turbulent flow conditions at the inlet plane ($x = 0$) are described in detail by Ferrante & Elghobashi (2004). Periodic boundary conditions were imposed only in the spanwise y-direction for the fluid velocity components and pressure. The no-slip condition for the fluid velocity ($U_1 = U_2 = U_3 = 0$) and Neumann condition for the pressure ($\partial_z p = 0$) were imposed at the wall boundary, $z = 0$. The Neumann (stress-free) condition for the fluid velocity components ($\partial_z U_2 = \partial_z U_3 = 0$) and Dirichlet condition ($U_1 = 1$ and $p = 0$) were imposed at the free-stream boundary, $z = L_z$. At the outflow plane ($x = L_x$) the convective condition, $\partial_t U_i + U_c\,\partial_x U_i = 0$, was imposed for the velocity components, where U_c is the instantaneous mean convective fluid velocity at the exit plane. A zero pressure gradient in the streamwise direction ($\partial_x p = 0$) was imposed at both the inflow and outflow planes. At time $t = 0$ the bubbles were released randomly in the computational domain inside the boundary layer zone ($z < \delta_0$), with each bubble velocity component set equal to that of the fluid at the bubble location. Bubble–bubble and bubble–wall collisions were neglected, since the instantaneous local maximum C rarely exceeded 10%, and a negligible number of bubbles comes in contact with the wall. In order to keep the average volume fraction of bubbles in the computational domain, ϕ_v, constant in time, when a bubble exits one of the domain boundaries it is reinjected at a random location inside the boundary layer according to a Gaussian distribution for the streamwise location, except for the spanwise boundaries ($y = 0$ and $y = L_y$) where periodicity was applied. The governing equations were discretized in space using a second-order finite difference scheme, except for the mean advection terms, which were evaluated via a fifth-order upwind differencing scheme. Time integration was performed using the second-order Adams–Bashforth scheme. The details of our numerical method are provided by Ferrante (2004). The bubble equation of motion, (2.3), was solved in time for each bubble using the Adams–Bashforth scheme to compute the bubble velocity. The fluid velocity, $\boldsymbol{U}_s$, fluid vorticity, $\boldsymbol{\omega}_s$, and fluid Lagrangian derivative, $\mathrm{D}\boldsymbol{U}_s/\mathrm{D}t$, at the bubble location were computed via a fourth-order-accurate fully three-dimensional Hermite cubic interpolation polynomial adapted to a non-uniform mesh (Ferrante 2004). The bubble positions were then updated from the time integration of the bubble velocity.

https://doi.org/10.1017/S0022112004007943 Published online by Cambridge University Press

	A	B	C	D	E	F	G	H
ϕ_v	0	0.001	0.01	0.01	0.02	0.02	0.001	0.001
N_B	0	8×10^5	8×10^6	8×10^6	16×10^6	16×10^6	8×10^5	8×10^5
g_i	–	$-g\,\delta_{iz}$	$-g\,\delta_{iz}$	$g\,\delta_{iz}$	$-g\,\delta_{iz}$	$g\,\delta_{iz}$	0	0
f_i	–	$\neq0$	$\neq0$	$\neq0$	$\neq0$	$\neq0$	$\neq0$	0
$\frac{C_{f,A}-C_f}{C_{f,A}}$	0	3.5%	11.7%	15.4%	14.1%	20.2%	3.8%	3.7%
$P_{u_{str}>0.04}$	8.5%	7.2%	5.5%	5.4%	4.9%	4.3%	7.8%	7.3%

TABLE 3. Physical parameters for the eight cases (A–H) studied and percentage reductions of skin friction and streak velocity.

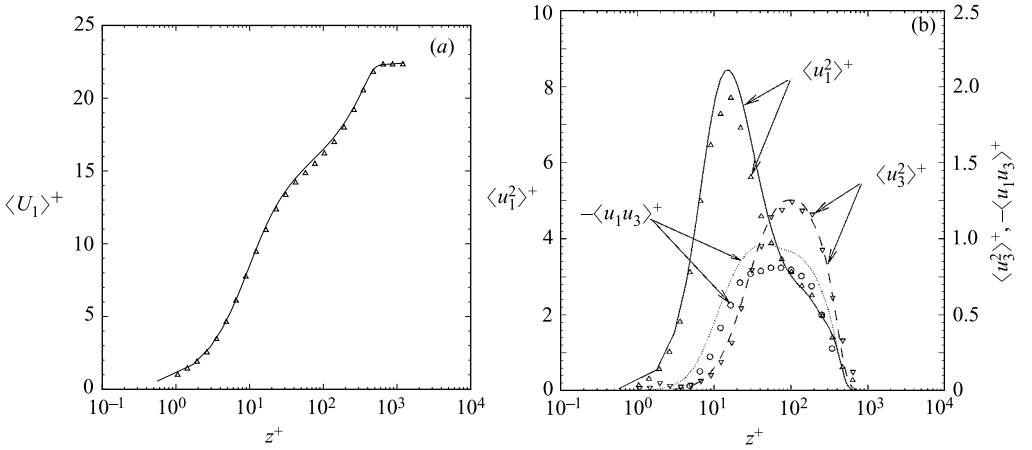


FIGURE 2. (*a*) Mean streamwise velocity profile and (*b*) Reynolds stresses profiles, at $Re_\theta = 1430$. Present DNS, case A (lines); experimental data of DeGraaff & Eaton (2000) (symbols).

3. Results

Table 1 shows the properties of the bubbles used in the present study. In tables 1 and 2 the variables written in wall units, and z_0^+ in figures 4–7, were non-dimensionalized using the friction velocity at the inflow plane, $u_\tau = 0.0464$ ($Re_\theta = 1020$) and $\nu = 1.25\times10^{-4}$. The parameters (ϕ_v, N_B, g_i and f_i) and the percentage reduction of skin friction in the eight test cases studied are listed in table 3. N_B is the total number of bubbles in the computational domain.

3.1. *Single-phase TBL: comparison with experiments*

We now compare our DNS results for the single-phase TBL (case A) with the experimental data of DeGraaff & Eaton (2000) for a spatially developing turbulent boundary layer over a flat plate at $Re_\theta = 1430$. We write the fluid velocity component, U_i, as the sum of its mean and fluctuation, $U_i(x, y, z, t) = \langle U_i\rangle(x, z) + u_i(x, y, z, t)$, where $\langle\ldots\rangle$ represents, throughout the paper, spatial averaging in the spanwise (y) direction in addition to time averaging of the enclosed quantity, and u_i is the local instantaneous deviation from $\langle U_i\rangle$. Figures 2(*a*) and 2(*b*) display the comparison in wall units for the mean streamwise velocity, $\langle U_1\rangle^+$, and three Reynolds stresses at $x = 18.8\delta_0$, where $Re_\theta = 1430$. The mean velocity profile is in excellent agreement with the experimental profile. The agreement for the normal Reynolds stresses $\langle u_1^2\rangle^+$ and

https://doi.org/10.1017/S0022112004007943 Published online by Cambridge University Press

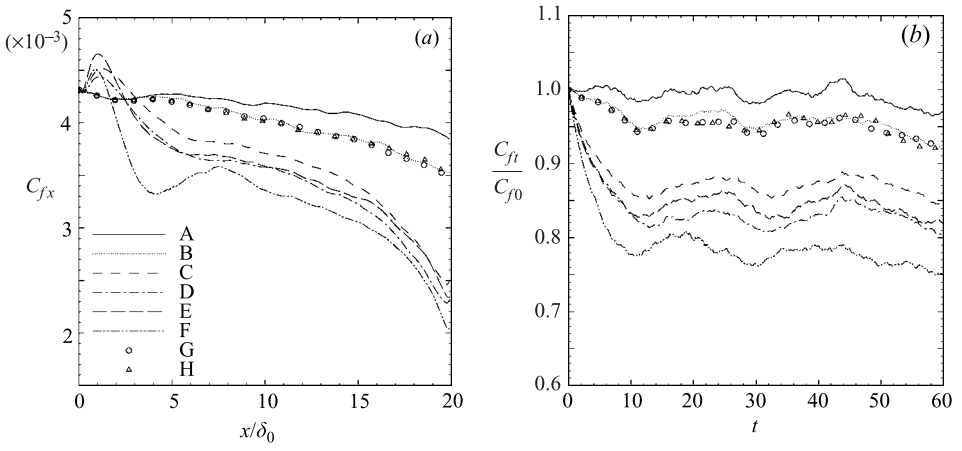


FIGURE 3. (*a*) Spatial development of C_{fx}; (*b*) temporal development of C_{ft}/C_{f0}.

$\langle u_3^2\rangle^+$ is very good. The difference in the magnitude of the peak of the turbulent shear stress, $\langle u_1u_3\rangle^+$, is probably due to experimental uncertainty. DeGraaff & Eaton (2000) indicate a 10% error in the measured value of $\langle u_1u_3\rangle^+$. A similar discrepancy was found by DeGraaff & Eaton (2000) in comparing their measurements with the DNS results of Spalart (1988) ($Re_\theta = 1410$). Our computed skin friction coefficient ($C_{fx} = 2\,\tau_w/(\rho\,U_\infty^2) = 3.96\times10^{-3}$, where $\tau_w = \mu[\partial_z\langle U_1\rangle(x,z)]_{z=0}$) at $Re_\theta = 1430$ is nearly identical to that measured ($C_{fx} = 3.97\times10^{-3}$) by DeGraaff & Eaton (2000).

3.2. *TBL laden with microbubbles*

The spatial streamwise development of the skin friction coefficient, C_{fx}, averaged in time and in the spanwise direction, is shown in figure 3(*a*). The temporal development of the skin friction coefficient, C_{ft}, averaged in both the spanwise and streamwise directions is shown in figure 3(*b*), normalized by its value at $t = 0$, C_{f0}. Table 3 shows the reduction of $C_f = (1/L_x)\int_0^{L_x} C_{fx}\mathrm{d}x$ and it ranges from 3.5% to 20.2% with respect to that in case A, $C_{f,A}$. In all the bubble-laden cases (B–H), C_{ft} is reduced at all times and C_{fx} is reduced at nearly all x locations in comparison to the single-phase TBL (case A). The reduction of C_{ft} is monotonic with increasing the average volume fraction, ϕ_v, of the bubbles for the same orientation of gravity (cases B, C and E, or D and F in figure 3*b*). For the plate-on-top cases (D and F), C_{ft} and C_{fx} are smaller than those for the plate-on-bottom cases (C and E) with the same ϕ_v. These results are in qualitative agreement with the experimental data of Madavan *et al.* (1984, 1985) and Pal *et al.* (1988) obtained at higher Reynolds numbers and higher bubbles volume fractions than those of the present study. In order to explain the physical mechanisms responsible for drag reduction in a bubble-laden TBL, we start by analysing the effects of microbubbles on the mean fluid velocity components. In accordance with the C_{fx} reduction, the mean streamwise fluid velocity, $\langle U_1\rangle$, is reduced in cases B–F compared to that in case A, as shown in figure 4(*a*), for the streamwise location $x = 18.8\delta_0$. Figure 4(*b*) shows the simultaneous increase of the mean vertical fluid velocity, $\langle U_3\rangle$, for cases B–F in comparison to case A.

In order to investigate how the microbubbles modify both $\langle U_1\rangle$ and $\langle U_3\rangle$, we note that mathematically there are only two sources attributed to the bubbles presence in the fluid continuity and momentum equations (2.1) and (2.2). The first is the coefficient $(1-C)$ and the other is the force term f_i. There is the additional external effect g_i in

https://doi.org/10.1017/S0022112004007943 Published online by Cambridge University Press

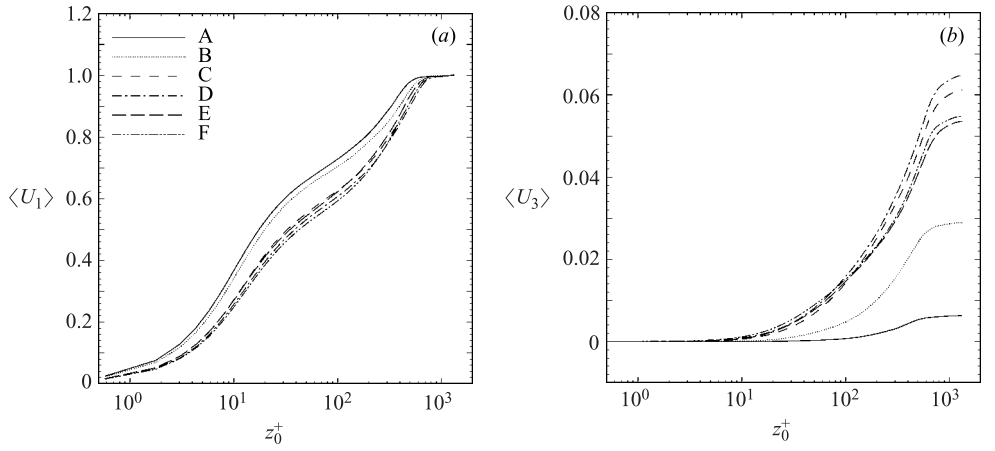


FIGURE 4. (*a*) Mean streamwise fluid velocity profile and (*b*) mean vertical fluid velocity profile, at $x = 18.8\delta_0$ (A–F).

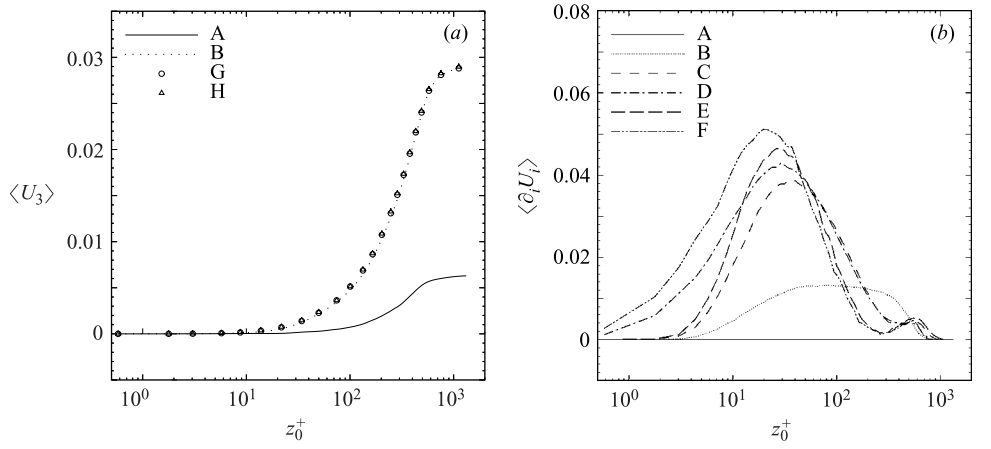


FIGURE 5. (*a*) Mean vertical fluid velocity profile (A, B, G and H) and (*b*) mean fluid velocity divergence, at $x = 18.8\delta_0$.

both the fluid momentum equation (2.1) and the bubble acceleration equation (2.3). We follow a step-by-step elimination process to examine the relative contribution of each of the above three factors (g_i, f_i and $(1 - C)$) to the drag reduction process. We first set the gravitational acceleration g_i to zero in case G. Figure 5(*a*) shows that $\langle U_3 \rangle$ for case G is almost identical to that of case B for the same volume fraction, $\phi_v = 0.001$. Figures 3(*a*) and 3(*b*) show that eliminating gravity has negligible effect on the drag reduction for the plate-on-bottom cases (B and G). Of course the results for plate-on-top cases (D and F) and plate-on-bottom cases (C and E) differ only due to the effects of gravity, owing to the tendency of bubbles to accumulate near the wall in the former cases (see figure 6*a*), as was observed in the experiments of Pal *et al.* (1988). Next, we set both the coupling force f_i and the gravitational acceleration g_i to zero in case H. Figures 3(*a*), 3(*b*) and 5(*a*) show that the distributions of C_{fx}, C_{ft} and $\langle U_3 \rangle$ in case B are nearly identical to those in case H. We conclude from the above two tests that the predicted drag reduction in our DNS results is caused almost entirely by the $(1 - C)$ coefficient in the fluid continuity and momentum equations.

https://doi.org/10.1017/S0022112004007943 Published online by Cambridge University Press

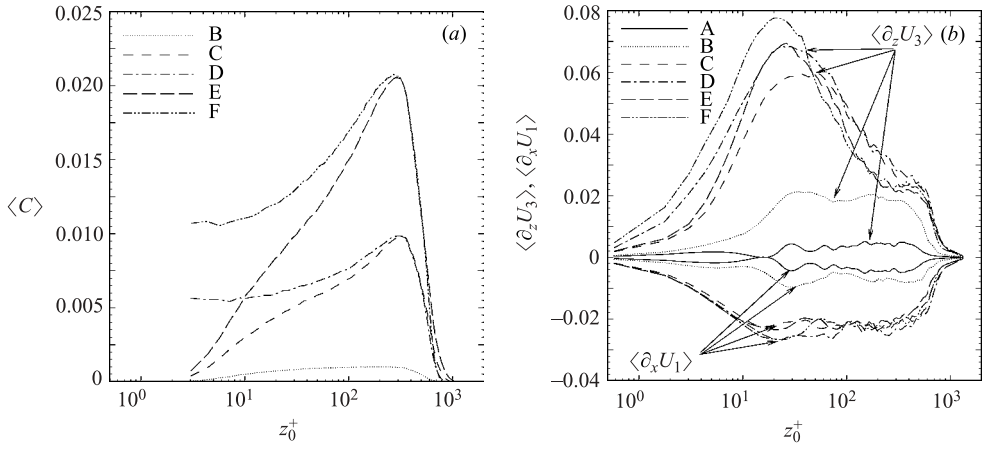


FIGURE 6. (*a*) Mean bubble concentration and (*b*) mean fluid velocity derivatives $\partial_z U_3$ and $\partial_x U_1$, at $x = 18.8\delta_0$.

We thus refer to the effect of $(1 - C)$ as the *velocity divergence effect* since the fluid continuity, (2.1), can be rewritten as:

$$\frac{\partial U_i}{\partial x_i} = \frac{1}{(1-C)} \frac{\mathrm{D}C}{\mathrm{D}t}. \tag{3.1}$$

Equation (3.1) indicates that if the local volume fraction of the bubbles, $C(x, y, z, t)$, increases, the fluid velocity divergence becomes positive, $\langle \partial_i U_i \rangle > 0$ (figure 5*b*), in the regions of the flow populated by bubbles (figure 6*a*). Furthermore, the well-established flow features in the single-phase TBL: $\langle \partial_z U_3 \rangle \geqslant 0$ and $\langle \partial_x U_1 \rangle \leqslant 0$ for $z \geqslant 0$ (figure 6*b*), and $\langle \partial_y U_2 \rangle = 0$, are still satisfied in the bubble-laden TBL. However, in contrast to the single-phase TBL, where $|\langle \partial_z U_3 \rangle| = |\langle \partial_x U_1 \rangle|$, we have in the bubble-laden TBL $|\langle \partial_z U_3 \rangle| \geqslant |\langle \partial_x U_1 \rangle|$ (figure 6*b*). The increase of $\langle \partial_z U_3 \rangle$ in the bubble-laden cases with respect to the single-phase flow (figure 6*b*) creates the larger $\langle U_3 \rangle$ (figure 4*b*), which in turn reduces $\langle U_1 \rangle$ (figure 4*a*).

Now, in order to explain how the $\langle U_3 \rangle$ created results in the reduction of the wall skin friction in the bubble-laden TBL, we first investigate the effect of $\langle U_3 \rangle$ on the near-wall coherent structures. We identify the quasi-streamwise vortical structures using the method of Jeong & Hussain (1995), who defined λ_2 as the second largest eigenvalue of the tensor $(S_{ik}S_{kj} + \Omega_{ik}\Omega_{kj})$, where $S_{ij} \equiv (\partial_j U_i + \partial_i U_j)/2$ is the strain rate tensor, and $\Omega_{ij} \equiv (\partial_j U_i - \partial_i U_j)/2$ is the rotation rate tensor. Jeong & Hussain (1995) showed that connected flow regions of negative values of λ_2 identify cores of vortical structures. We applied this method to our TBL flow, and observed that the vortical structures populating the buffer layer in the bubble-laden TBL remain inclined almost in the streamwise direction (quasi-streamwise vortical structures) as in the single-phase TBL. This was indicated by the profiles (not shown) of the correlation coefficients, R_i (Jeong *et al.* 1997), between $-\lambda_2$ and the absolute values of the vorticity components, ω_i, as they remain nearly identical for the different cases A–F. The vortical structures are oriented nearly in the streamwise direction x for both the single-phase and bubble-laden TBL, since R_x is larger than R_y and R_z inside the buffer layer ($10 < z_0^+ < 40$), where the near-wall coherent structures are located (Jeong *et al.* 1997).

https://doi.org/10.1017/S0022112004007943 Published online by Cambridge University Press

Case	A	B	C	D	E	F
$(\lambda_2')_{max}$	3.12	2.77	2.54	2.63	2.42	2.65
z^+_{peak}	19.6	21.8	24.0	24.0	26.4	26.4

TABLE 4. $(\lambda_2')_{max}$, and vertical location of this maximum value, z^+_{peak}, at $x = 18.8\delta_0$.

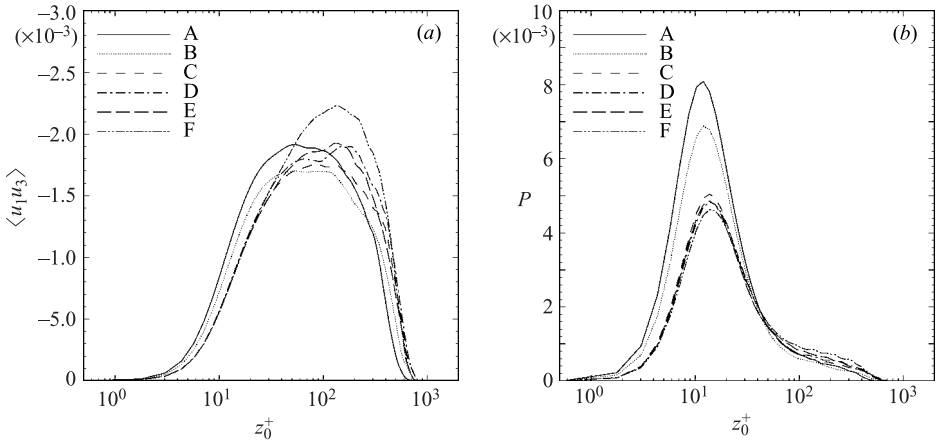


FIGURE 7. (*a*) Fluid velocity correlation between the streamwise and vertical components, $\langle u_1 u_3 \rangle$, and (*b*) production of turbulence kinetic energy, at $x = 18.8\delta_0$.

Large values of λ_2' (r.m.s. of λ_2) indicate flow regions populated by quasi-streamwise vortical structures (Jeong *et al.* 1997). Table 4 indicates that the peaks of λ_2' are reduced and shifted away from the wall for the bubble-laden flow cases relative to those of case A, in response to the increased $\langle U_3 \rangle$. The shifting of the vortical structures away from the wall indicates that the 'sweep' and 'ejection' events, which are located respectively at the downward and upward sides of these longitudinal vortical structures, are moved farther away from the wall compared to those in case A. Thus, the intensity of the 'wall streaks' is reduced in the bubble-laden cases. Table 3 displays the values of probability, $P_{u_{str}>0.04}$, that the streamwise velocity in the plane nearest to the wall exceeds 50% of its maximum value. Case A has the largest value whereas case F has the smallest. Since the downward and upward flow regions at the sides of a rotating vortical structure are characterized by instantaneous negative values of the product $U_1 U_3$, then the shifting of these structures away from the wall in the bubble-laden TBL moves the peak of $\langle u_1 u_3 \rangle$ towards higher z location (figure 7*a*) compared to that of case A. Now the reduction of $\langle U_1 \rangle$ near the plate (figure 4*a*), decreases $\partial_z \langle U_1 \rangle$ for $z_0^+ < 20$. Thus, the combined effect of the shifting of $\langle u_1 u_3 \rangle$ towards larger values of z and the reduction of $\partial_z \langle U_1 \rangle$, reduces the production of the turbulence kinetic energy (TKE), $\mathscr{P} = -\langle u_1 u_3 \rangle \partial_z \langle U_1 \rangle$, shown in figure 7(*b*). Consequently, the peaks of TKE and enstrophy, $\langle \omega_i^2 \rangle$, (not shown) are reduced and shifted towards higher z locations in the bubble-laden cases.

4. Discussion

Our DNS results for a microbubble-laden TBL with volume fraction ranging from $\phi_v = 0.001$ to 0.02 show that the presence of bubbles results in a local positive

https://doi.org/10.1017/S0022112004007943 Published online by Cambridge University Press

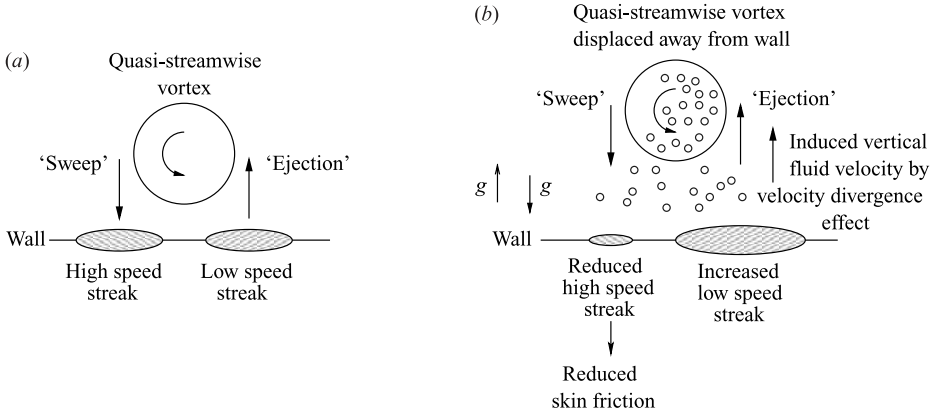


FIGURE 8. Schematic of the drag reduction mechanism in a bubble-laden TBL: (*a*) Single-phase flow, (*b*) bubble-laden flow.

divergence of the fluid velocity, $\nabla \cdot \boldsymbol{U} > 0$, creating a positive mean velocity, $\langle U_3 \rangle$, normal to (and away from) the wall which, in turn, reduces the mean streamwise velocity and displaces the quasi-streamwise longitudinal vortical structures away from the wall as in figure 8. This displacement has two main effects. (i) It increases the spanwise gaps between the wall streaks associated with the sweep events and reduces the streamwise velocity in these streaks, thus reducing the skin friction by up to 20.2% for $\phi_v = 0.02$ (case F). (ii) It moves the location of peak Reynolds stress production away from the wall to a zone of a smaller transverse gradient of the mean streamwise velocity (i.e. smaller mean shear), thus reducing the production rate of turbulence kinetic energy and enstrophy.

REFERENCES

AUTON, T. R. 1987 The lift force on a spherical body in a rotational flow. *J. Fluid Mech.* **183**, 199–218.

CLARK III, H. & DEUTSCH, S. 1991 Microbubble skin friction on an axisymmetric body under the influence of applied axial pressure gradients. *Phys. Fluids* A **3**, 2948–2954.

DEGRAAFF, D. B. & EATON, J. K. 2000 Reynolds-number scaling of the flat-plate turbulent boundary layer. *J. Fluid Mech.* **422**, 319–346.

DEUTSCH, S. & PAL, S. 1990 Local shear stress measurements on an axisymmetrical body in a microbubble-modified flow field. *Phys. Fluids* A **2**, 2140–2146.

DRUZHININ, O. A. & ELGHOBASHI, S. 1998 Direct numerical simulation of bubble-laden turbulent flows using the two fluid formulation. *Phys. Fluids* **10**, 685–697.

FERRANTE, A. 2004 Reduction of skin friction in a microbubbles-laden spatially-developing turbulent boundary layer over a flat plate. PhD thesis, University of California, Irvine.

FERRANTE, A. & ELGHOBASHI, S. 2004 A robust method for generating inflow conditions for direct simulations of spatially-developing turbulent boundary layers. *J. Comput. Phys.* (in press).

JEONG, J. & HUSSAIN, F. 1995 On the identification of a vortex. *J. Fluid Mech.* **285**, 69–94.

JEONG, J., HUSSAIN, F., SCHOPPA, W. & KIM, J. 1997 Coherent structures near the wall in a turbulent channel flow. *J. Fluid Mech.* **332**, 185–214.

MCCORMICK, M. & BHATTACHARYYA, R. 1973 Drag reduction of a submersible hull by electrolysis. *Nav. Engg J.* **85**, 11.

MADAVAN, N., DEUTSCH, S. & MERKLE, C. 1984 Reduction of turbulent skin friction by microbubbles. *Phys. Fluids* **27**, 356–363.

MADAVAN, N., DEUTSCH, S. & MERKLE, C. 1985 Measurements of local skin friction in a microbubble-modified turbulent boundary-layer. *J. Fluid Mech.* **27**, 237–256.

https://doi.org/10.1017/S0022112004007943 Published online by Cambridge University Press

Maxey, M. R. & Riley, J. 1983 Equation of motion for a small rigid sphere in a turbulent fluid flow. *Phys. Fluids* **26**, 883–889.

Pal, S., Merkle, C. & Deutsch, S. 1988 Bubble characteristics and trajectories in a microbubble boundary layer. *Phys. Fluids* **31**, 744–751.

Prosperetti, A. & Zhang, D. Z. 1995 Finite-particle-size effects in disperse tho phase flows. *Theoret. Comput. Fluid Dyn.* **7**, 429–440.

Spalart, P. R. 1988 Direct simulation of a turbulent boundary layer up to $Re_\theta = 1410$. *J. Fluid Mech.* **187**, 61–98.

Xu, J., Maxey, M. & Karniadakis, G. 2002 Numerical simulation of turbulent drag reduction using micro-bubbles. *J. Fluid Mech.* **468**, 271–281.

https://doi.org/10.1017/S0022112004007943 Published online by Cambridge University Press